

# A Virgo Environmental Survey Tracing Ionised Gas Emission (VESTIGE)

## XI. Two-dimensional $H\alpha$ kinematics of the edge-on ram pressure stripped galaxy NGC 4330<sup>★,★★</sup>

M. M. Sardaneta<sup>1</sup>, P. Amram<sup>1</sup>, A. Boselli<sup>1</sup>, B. Vollmer<sup>2</sup>, M. Rosado<sup>3</sup>, M. Sánchez-Cruces<sup>1,3</sup>, A. Longobardi<sup>4</sup>, C. Adami<sup>1</sup>, M. Fossati<sup>4</sup>, B. Epinat<sup>1</sup>, M. Boquien<sup>5</sup>, P. Côté<sup>6</sup>, G. Hensler<sup>7</sup>, Junais<sup>1</sup>, H. Plana<sup>8</sup>, J. C. Cuillandre<sup>9</sup>, L. Ferrarese<sup>6</sup>, J. L. Gach<sup>1</sup>, J. A. Gomez-Lopez<sup>1</sup>, S. Gwyn<sup>6</sup>, and G. Trinchieri<sup>10</sup>

<sup>1</sup> Aix-Marseille Univ., CNRS, CNES, LAM, Marseille, France

e-mail: [minerva.munoz@lam.fr](mailto:minerva.munoz@lam.fr), [philippe.amram@lam.fr](mailto:philippe.amram@lam.fr), [alessandro.boselli@lam.fr](mailto:alessandro.boselli@lam.fr)

<sup>2</sup> Université de Strasbourg, CNRS, Observatoire astronomique de Strasbourg, UMR 7550, 67000 Strasbourg, France

<sup>3</sup> Instituto de Astronomía, Universidad Nacional Autónoma de México, Apartado Postal 70-264, Coyoacán, Ciudad de México 04510, Mexico

<sup>4</sup> Università di Milano-Bicocca, piazza della scienza 3, 20100 Milano, Italy

<sup>5</sup> Centro de Astronomía (CITEVA), Universidad de Antofagasta, Avenida Angamos 601, Antofagasta, Chile

<sup>6</sup> National Research Council of Canada, Herzberg Astronomy and Astrophysics, 5071 West Saanich Road, Victoria, BC V9E 2E7, Canada

<sup>7</sup> Department of Astrophysics, University of Vienna, Türkenschanzstrasse 17, 1180 Vienna, Austria

<sup>8</sup> Laboratório de Astrofísica Teórica e Observacional, Universidade Estadual de Santa Cruz, 45650-000 Ilhéus-BA, Brazil

<sup>9</sup> AIM, CEA, CNRS, Université Paris-Saclay, Université Paris Diderot, Sorbonne Paris Cité, Observatoire de Paris, PSL University, 91191 Gif-sur-Yvette Cedex, France

<sup>10</sup> INAF – Osservatorio Astronomico di Brera, via Brera 28, 20159 Milano, Italy

Received 21 September 2021 / Accepted 17 December 2021

### ABSTRACT

Using the VESTIGE survey, a deep narrow-band  $H\alpha$  imaging survey of the Virgo cluster carried out at the CFHT with MegaCam, we discovered a long and diffuse tail of ionised gas in the edge-on late-type galaxy NGC 4330. This peculiar feature indicates an ongoing ram pressure stripping event able to remove the gas in the outer region of the disc. Tuned hydrodynamic simulations suggest that the ram pressure stripping event is occurring almost face-on, making NGC 4330 the ideal candidate for studying the effects of the perturbation in the direction perpendicular to the disc plane. We present here two new independent sets of Fabry-Perot observations ( $R \approx 10\,000$ ) with the purpose of understanding the effects of the ram pressure stripping process on the kinematics of the ionised gas. Despite their limited sensitivity to the diffuse gas emission, the data allowed us to measure the velocity and the velocity dispersion fields over the galaxy disc and in several features at the edges or outside the stellar disc formed after the ram pressure stripping event. We constructed the position-velocity diagrams and the rotation curves of the galaxy using three different techniques. The data show, consistent with the hydrodynamic simulations, that the galaxy has an inner solid-body rotation up to  $\sim 2.4$  kpc, with non-circular streaming motions outside this radius and in the several external features formed during the interaction of the galaxy with the surrounding intracluster medium. The data also indicate a decrease in the rotational velocity of the gas with increasing distance from the galaxy disc along the tails, suggesting a gradual but not linear loss of angular momentum in the stripped gas. Consistent with a ram pressure stripping scenario, the  $i$ -band image shows a boxy shape at the south-west edge of the disc, where the stellar orbits might have been perturbed by the modification of the gravitational potential well of the galaxy due to the displacement of the gas in the  $z$  direction.

**Key words.** galaxies: clusters: general – galaxies: clusters: individual: Virgo – galaxies: evolution – galaxies: interactions – galaxies: kinematics and dynamics

\* Reduced datacubes are also available at the CDS via anonymous ftp to [cdsarc.u-strasbg.fr](ftp://cdsarc.u-strasbg.fr) (130.79.128.5) or via <http://cdsarc.u-strasbg.fr/viz-bin/cat/J/A+A/659/A45>

\*\* Based on observations obtained: (1) at the Observatoire de Haute Provence (OHP; France), operated by the French Centre National de la Recherche Scientifique (CNRS); (2) at the Observatorio Astronómico Nacional in San Pedro Mártir, Baja California, Mexico (OAN-SPM); and with (3) MegaPrime/MegaCam, a joint project of CEA/DAPNIA and the Canada-French-Hawaii Telescope (CFHT), which is operated by the National Research Council (NRC) of Canada, the Institut National des Sciences de l'Univers of the CNRS of France, and the University of Hawaii.

## 1. Introduction

The environment plays a major role in shaping galaxy evolution (e.g., Peng et al. 2010). Rich clusters are dominated by quiescent systems (morphology-segregation effect; Dressler 1980), and the few spirals that inhabit these environments are generally deficient in all the components of their interstellar medium (ISM; HI – Cayatte et al. 1990; Solanes et al. 2001; Gavazzi et al. 2005; Chung et al. 2009; H<sub>2</sub> – Fumagalli et al. 2009; Boselli et al. 2014a; dust – Cortese et al. 2010, 2012b; Longobardi et al. 2020). Their star formation is also reduced with respect to that of similar objects in the field (Gavazzi et al. 1998, 2002a,b, 2006, 2010, 2013; Lewis et al. 2002; Gómez et al. 2003; Peng et al. 2010; Boselli et al. 2014b, 2016b; Cortese et al. 2021).

Different physical mechanisms have been proposed in the literature to explain these results, as extensively reviewed in Boselli & Gavazzi (2006, 2014). These include gravitational interactions with other cluster members (Merritt 1983) or with the gravitational potential well of the cluster (Byrd & Valtonen 1990) – including their combined effect, generally called galaxy harassment (Moore et al. 1998) – or the hydrodynamic interaction of the ISM of galaxies with the hot and dense intracluster gas (thermal evaporation, Cowie & Songaila 1977; starvation, Larson et al. 1980; ram pressure stripping, Gunn et al. 1972). Several observations seem to indicate that while gravitational perturbations are dominant in relatively small systems such as groups thanks to the low velocity dispersion of galaxies within the dark matter halo, hydrodynamic interactions are dominant in massive clusters, where the high velocity dispersion and the density of the gas make them particularly efficient (e.g., Vollmer et al. 2001; Boselli et al. 2008a,b, 2014a; Gavazzi et al. 2013). It is nevertheless clear that all these different perturbing mechanisms might be acting jointly on galaxies in rich environments, with different effects on their evolution.

Despite this evolutionary picture is becoming clearer, there are still several aspects of the galaxy transformation in rich environments that are poorly known. Among these is the fate of the ISM removed during a ram pressure stripping event. The stripped ISM is often observed in spectacular tails of atomic (e.g., Chung et al. 2007), ionised (e.g., Gavazzi et al. 2001; Yagi et al. 2010; Boselli et al. 2016a), or hot gas (e.g., Sun et al. 2007). Indeed, it has been observed that while in some objects the stripped gas collapses within the tail to form giant molecular clouds (Jáchym et al. 2014, 2017, 2019; Moretti et al. 2020) and stars (Fossati et al. 2016; Poggianti et al. 2019), in other systems it remains diffuse (e.g., Boissier et al. 2012). In these objects the cold gas stripped from the disc does not form stars because it changes phase, becoming first ionised then hot (e.g., Boselli et al. 2016a). The detailed analysis of a few nearby systems with high quality multi-frequency spectroscopic and imaging data seems to suggest that the gas collapses into giant molecular clouds only when its velocity dispersion is sufficiently low (e.g., Fossati et al. 2016; Boselli et al. 2018b). Otherwise, the cold gas changes phase for heat conduction, turbulence, magneto-hydrodynamic waves, or shocks. It thus becomes first ionised and then hot gas visible in the X-ray spectral domain (Gavazzi et al. 2001; Sun et al. 2007; Fossati et al. 2016; Boselli et al. 2016a).

The kinematics of the stripped gas is thus a crucial parameter for understanding the process of star formation within the tails. Observations and simulations of ram pressure stripped galaxies consistently indicate that a ram pressure stripping process is able to drastically perturb the velocity field of a spiral galaxy, displacing its kinematic centre with respect to the photometric one and affecting its rotation curve (RC; Vollmer

et al. 2001, 2004, 2006, 2008; Kronberger et al. 2008; Merluzzi et al. 2013; Fumagalli et al. 2014; Consolandi et al. 2017; Sheen et al. 2017; Bellhouse et al. 2017, 2019; Boselli et al. 2022). Despite the advent of extraordinary new instrumentation in the optical (Multi Unit Spectroscopic Explorer (MUSE) at the Very Large Telescope (VLT)) and radio (Atacama Large Millimeter/submillimeter Array – ALMA) domain, multi-frequency data at high angular and spectral resolution of nearby ram pressure stripped galaxies, where the proximity allows us to study the star formation process down to the scale of individual HII regions, are only sporadically available. To understand the effects of the stripping process on the kinematics of the gas, observations and simulations of galaxies spanning a wide range in stellar mass and with different impact parameters are necessary. A particularly interesting case are edge-on galaxies, which allow us to observe as the gas is stripped out from the disc plane in the  $z$  direction. Among these, there are only two systems undergoing a ram pressure stripping event that have been studied in detail: UGC 6697 in the cluster A1367 (Consolandi et al. 2017) and JO204 in the farther cluster, A957 ( $z \sim 0.052$ ; Gullieuszik et al. 2017). The kinematic properties of the stripped gas are significantly different in the two galaxies given their impact parameters, UGC 6697 suffering an edge-on stripping event and JO204 a face-on one.

The Virgo Environmental Survey Tracing Ionised Gas Emission (VESTIGE; Boselli et al. 2018c), a blind H $\alpha$  narrow-band imaging survey of Virgo, allows us to identify a large number of galaxies undergoing a ram pressure stripping event in the closest cluster of galaxies. The presence of ionised gas tails without any stellar counterpart is the clearest demonstration that a system is undergoing a hydrodynamic interaction with the surrounding environment. Indeed, gravitational perturbations act indifferently on the stellar and gaseous components, also producing tidal structures visible in deep broad-band imaging data. Several galaxies undergoing a ram pressure stripping event have been identified so far (Boselli et al. 2016a, 2018a, 2022; Fossati et al. 2018; Longobardi et al. 2020; Junais et al. 2021). Among them, NGC 4330 is an edge-on galaxy with evident tails of atomic (Chung et al. 2007, 2009) and ionised (Abramson et al. 2011; Fossati et al. 2018) gas, which indicates that the galaxy is entering the cluster from the south and impacting the intracluster medium (ICM) almost face on. It is thus an ideal candidate for studying in great detail the effects of the perturbation on the kinematics of the perturbed gas on the disc of the galaxy and within the tail.

In this paper we use two different sets of high spectral resolution (up to  $R \simeq 10000$ ) Fabry-Perot (FP) data to study the kinematics of the ionised gas in this representative object. We combine these new sets of observations with tuned hydrodynamic simulations developed to reproduce the structural and spectrophotometric properties of this galaxy (Vollmer et al. 2021). Unfortunately, most of the gas in the tail has a very low surface brightness, and thus it is out of reach for our dedicated observations, which detect only a few high-surface-brightness star-forming regions. The proximity of the galaxy (16.5 Mpc; Gavazzi et al. 1999; Mei et al. 2007), however, and the adopted spectral resolution allow us to study in detail the kinematics of the gas of these compact regions down to scales of  $\sim 100$  pc in angular resolution and velocity dispersion  $\sigma \sim 13$  km s<sup>-1</sup>. Such resolution is not reached for the more distant UGC 6697 and JO204 despite their extraordinary MUSE data.

The paper is structured as follows: in Sect. 2 we describe the MegaCam Canada-French-Hawaii Telescope (CFHT) narrow-band imaging and the FP high-resolution spectroscopic

observations along with the multi-frequency data used in the analysis. In Sects. 3 and 4 we analyse the imaging data and construct the RC of the galaxy, while we study the two-dimensional kinematics of the gas in Sect. 5 and the specific kinematics of the gas out of the plane in Sect. 6. The results of the analysis are compared to the hydrodynamic simulations of Vollmer et al. (2021) in Sect. 7. The discussion and conclusions are given in Sect. 8.

## 2. Observations and data reduction

### 2.1. VESTIGE narrow-band imaging

Deep H $\alpha$  narrow-band imaging of NGC 4330 has been gathered with MegaCam at the CFHT by the VESTIGE survey (Boselli et al. 2018c), and the first imaging results have been presented in Fossati et al. (2018). Briefly, the galaxy has been observed using the narrow-band filter MP9603 ( $\lambda_c = 6591 \text{ \AA}$ ;  $\Delta\lambda = 106 \text{ \AA}$ ), which includes the H $\alpha$  line and the two [NII] lines at  $\lambda 6548 \text{ \AA}$  and  $\lambda 6584 \text{ \AA}$ <sup>1</sup>. The galaxy has been observed during the main VESTIGE survey but also during a pilot run. The data used in this work are the combination of these two datasets, and are thus deeper than those analysed in Fossati et al. (2018), which were limited to the pilot observations. To secure the subtraction of the stellar continuum, the galaxy has been also observed in the broad  $r$ -band filter with shorter exposures to avoid saturation within the nucleus. The different exposures were gathered using a large dither pattern (15 arcmin in RA and 20 arcmin in Dec) to minimise the effects of scattered light and reflections in the flat-fielding, thus optimising the detection of low-surface-brightness features in the ionised gas component. A slightly different pattern was used for the pilot observations. The total integration time is 21060 sec in the narrow-band filter and 1506 sec in the broad-band  $r$  filter<sup>2</sup>. These deep observations have a typical sensitivity of  $f(\text{H}\alpha) \simeq 2 \times 10^{-17} \text{ erg s}^{-1} \text{ cm}^{-2}$  ( $5\sigma$ ) for point sources and  $\Sigma(\text{H}\alpha) \simeq 10^{-18} \text{ erg s}^{-1} \text{ cm}^{-2} \text{ arcsec}^{-2}$  ( $1\sigma$  after smoothing the data to  $\sim 3 \text{ arcsec}$  resolution) for extended sources, thus approximately a factor of 1.7 deeper than the mean sensitivity of VESTIGE. NGC 4330 has been observed during excellent seeing conditions ( $FWHM = 0.73 \text{ arcsec}$ ).

The data have been reduced using Elixir-LSB (Ferrarese et al. 2012), a data reduction pipeline especially designed to detect the diffuse emission of extended low-surface-brightness structures formed during the interaction of galaxies with their surrounding environment (e.g., Boselli et al. 2016b). The astrometric and photometric calibrations have been done using the Sloan Digital Sky Survey (SDSS) and the Panoramic Survey Telescope and Rapid Response System (Pan-STARRS) surveys by means of the MegaPipe pipeline (Gwyn 2008). The typical photometric uncertainty in the data is of 0.02–0.03 mag in both bands. The emission of the ionised gas has been derived after subtracting the stellar continuum as described in Boselli et al. (2019). This is done by combining the  $r$ -band image with the  $g$ -band frame obtained during the Next Generation Virgo Cluster Survey (NGVS; Ferrarese et al. 2012) to take the colour of the stellar continuum into account (Spector et al. 2012).

<sup>1</sup> Hereafter we refer to the H $\alpha$ + [NII] band simply as H $\alpha$ , unless otherwise stated.

<sup>2</sup> The total integration time in the  $r$ -band filter reported in Fossati et al. (2018) includes archival data not considered here, for the sake of consistency with the rest of the VESTIGE survey.

### 2.2. Fabry-Perot spectroscopy

High-resolution Integral Field Unit (IFU) spectroscopy was obtained using two different FP interferometers, PUMA attached at the 2.1 m telescope in San Pedro Mártir, Baja California, Mexico, and GHASP, mounted on the 1.93 m telescope at the Observatoire de Haute Provence (OHP), France. A detailed description of the instruments, of the observations, and of the data reduction is given in Appendix A. Briefly, PUMA is an FP spectrograph with a field of view of  $\sim 10 \times 10 \text{ arcmin}^2$  coupled with a  $512 \times 512$  charge-coupled device (CCD) camera, with pixel size of  $1.27 \times 1.27 \text{ arcsec}^2$  and has a spectral resolution  $R \sim 6500$ . GHASP has a field of view of  $5.8 \times 5.8 \text{ arcmin}^2$ , is coupled with a  $512 \times 512$  Image Photon Counting System (IPCS) with pixel size of  $0.68 \times 0.68 \text{ arcsec}^2$ , and has a spectral resolution  $R \sim 10000$ .

### 2.3. Multi-frequency data

The FP data were combined to those gathered during other surveys of the Virgo cluster for the following analysis, as extensively described in Fossati et al. (2018). Namely, the distribution of the old stellar population has been derived using the very deep  $i$ -band image obtained during the NGVS survey of the cluster (Ferrarese et al. 2012). HI data are also available from the Imaging of Virgo Spirals in Atomic Gas (VIVA), gathered at the Very Large Array (VLA) in C-short array configuration (Chung et al. 2009). These data have been obtained with a velocity sampling of  $\sim 10 \text{ km s}^{-1}$  and a spatial resolution of  $\sim 15 \text{ arcsec}$ . The same set of data has been combined with other VLA data obtained in D configuration to increase the sensitivity to low column density, extended features by Abramson et al. (2011) with a final velocity resolution of  $10.4 \text{ km s}^{-1}$  and an angular resolution of full width at half maximum (FWHM) of  $26.4 \times 24.0 \text{ arcsec}^2$ . <sup>12</sup>CO(2–1) observations obtained with the Submillimeter Array (SMA), with a synthesised beam of  $6.35 \times 4.47 \text{ arcsec}^2$  and a spectral resolution of  $5 \text{ km s}^{-1}$ , have been presented in Lee et al. (2017).

## 3. Imaging analysis

### 3.1. Stellar distribution

The NGVS  $i$ -band image (see Fig. 1) traces the bulk of the stellar population and can thus be used to derive the main morphological and structural parameters of the galaxy. It can also be used as reference to identify the different ionised gas structures removed from the disc plane during the interaction. This image shows an edge-on disc with a symmetric and unperturbed stellar distribution down to the surface brightness limit of the NGVS survey ( $\mu_i = 27.4 \text{ mag arcsec}^{-2}$ ), proving that the galaxy is not undergoing any major gravitational perturbation. The galaxy has a small bulge without any evident bar (e.g., Abramson et al. 2011).

We derived the photometric properties of the stellar disc through the elliptical isophote fitting method using the IRAF task ELLIPSE (Jedrzejewski 1987). In this task, ellipses are drawn to match the isophotes. The surface brightness along the ellipse is expanded in Fourier series:

$$\mu(\theta) = \mu_0 + \sum_{n=1, \infty} (A_n \sin n\theta + B_n \cos n\theta), \quad (1)$$

where  $\mu_0$  is the surface brightness averaged over the ellipse,  $A_n$  and  $B_n$  the higher order Fourier coefficients. If an isophote is a perfect ellipse, all the  $A_n$  and  $B_n$  coefficient would be exactly zero. The term  $A_1$ ,  $B_1$ ,  $A_2$ , and  $B_2$  indicate errors in the fitting

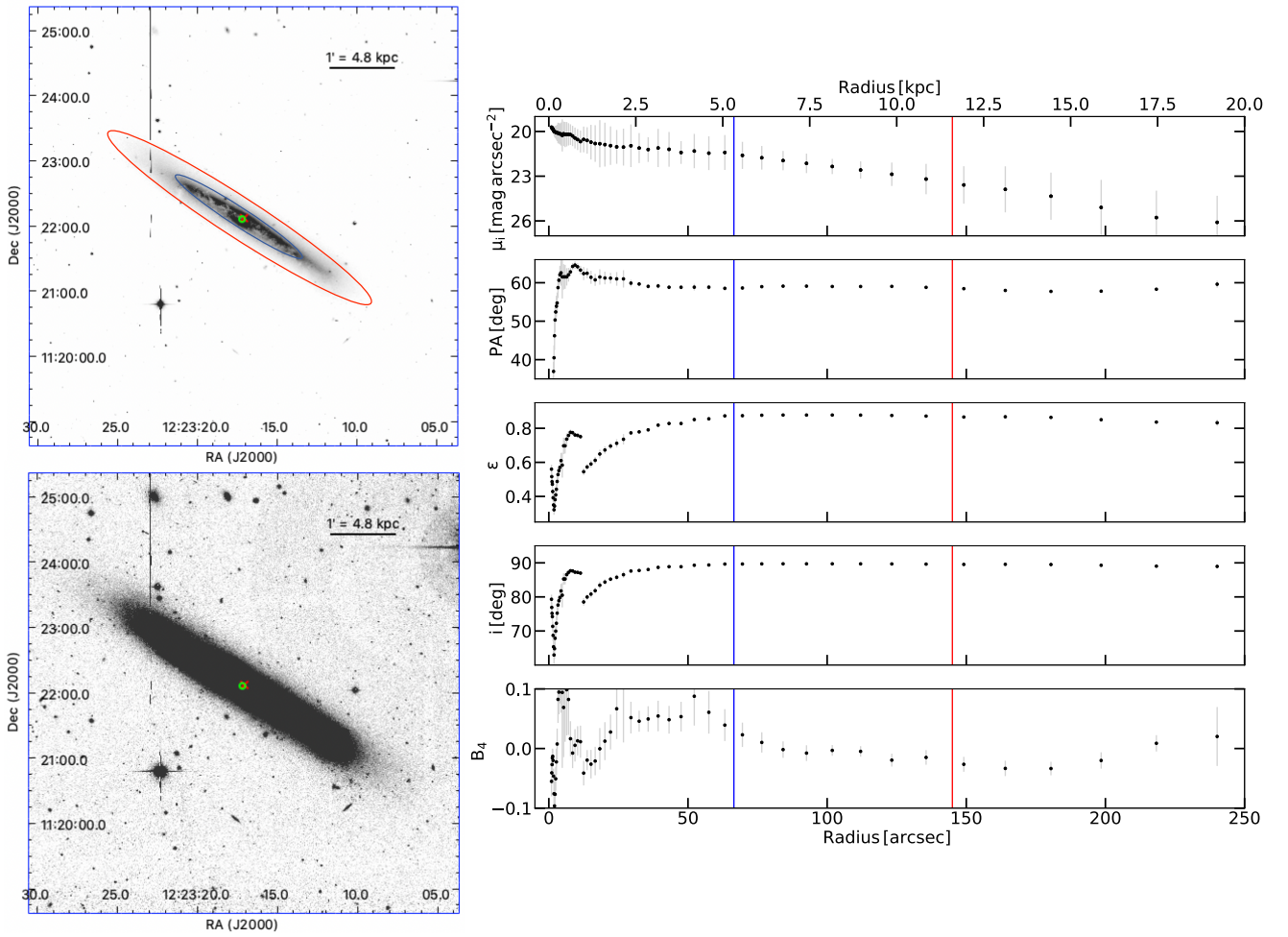


**Fig. 1.** Photometric properties of NGC 4330. *Left panels:* NGVS *i*-band image at low contrast (*upper panel*) to see the distribution of the absorbing dust within the disc, and at high contrast in logarithmic scale (*lower panel*) to see the boxy shape of the disc at its edges. The red and blue ellipses indicate the *i*-band mean surface brightness  $\mu(i) = 23.5$  and the effective surface brightness  $\mu_e = 21.5$  mag arcsec<sup>-2</sup>, respectively. The green bullet and the red cross indicate the position of the photometric and kinematical centres, respectively. *Right panels, from top to bottom:* radial variation in the *i*-band surface brightness ( $\mu$ ), position angle (*PA*), ellipticity ( $\epsilon$ ), morphological inclination ( $i_{\text{ph}}$ ), and the fourth degree cosine coefficient of the Fourier series ( $B_4$ ) parameters. The red and blue vertical lines correspond to the ellipses drawn in the upper left panel and indicate the radius  $R_{23.5}(i) \sim 145.0$  arcsec ( $\sim 11.6$  kpc) and the effective radius  $R_e(i) \sim 66.5$  arcsec ( $\sim 5.3$  kpc), respectively.

procedure. The terms  $A_3$  and  $B_3$  give the ‘egg-shaped’ isophote but the most interesting is  $B_4$ . If  $B_4 > 0$ , the galaxy has discy-shape isophotes, while if  $B_4 < 0$  boxy-shaped isophotes. The ELLIPSE task provides a number of parameters that describe the surface brightness of the galaxy as a function of the semi-major axis, including the ellipticity ( $\epsilon$ ), the position angle (*PA*), and it reconstructs the growth curve that gives the total apparent magnitude inside each isophote (e.g., [Barbosa et al. 2015](#); [Korsaga et al. 2019](#)). All these parameters were allowed to vary as a function of the radial distance from the galaxy centre.

The isophotal radius derived using the NGVS *i*-band image is  $R_{23.5}(i) \sim 145.0$  arcsec ( $\sim 11.6$  kpc). This value is slightly larger than the one derived by [Cortese et al. \(2012a\)](#) using the SDSS-*i*-band image ( $R_{23.5}(i) \sim 140.3$  arcsec,  $\sim 11.2$  kpc). The difference with this previous measurement might be due to the presence of dust and to the adopted sigma clipping selection in the ELLIPSE task. The effective radius is  $R_e(i) \sim 66.5$  arcsec ( $\sim 5$  kpc) and the effective surface brightness  $\mu_e(i) \sim 21.5$  mag arcsec<sup>-2</sup>, consistently with those given in [Cortese et al. \(2012a\)](#). The photometric centre is located at RA(J2000) = 12<sup>h</sup>23<sup>m</sup>17.26<sup>s</sup>, Dec = +11°22′07″.9, with an

uncertainty of  $\sim 0.9$  arcsec ( $\sim 76$  pc). The sudden jump of the parameters observed in Fig. 1 at a radius of  $\sim 5$  arcsec ( $\sim 0.4$  kpc) is due to the dusty region around the centre.

Consistently with, for example, [Barbosa et al. \(2015\)](#), we estimate the morphological inclination of the galaxy using the relation

$$\cos i_{\text{ph}} = \frac{(1 - \epsilon)^2 - q_0^2}{1 - q_0^2}, \quad (2)$$

where  $q_0 = 0.1$  is the intrinsic flattening of a Scd galaxy ([Haynes & Giovanelli 1984](#)). Figure 1 indicates that the morphological inclination of the galaxy converges to  $i_{\text{ph}} = 89.5^\circ$  and the photometric position angle to  $PA_{\text{ph}} = 59 \pm 1^\circ$  for  $R(i) \geq 75$  arcsec ( $\sim 6$  kpc) ( $\mu_i \geq 22.75$  mag arcsec<sup>-2</sup>). The  $B_4$  parameter, which is negative, indicates that the galaxy disc has a boxy shape outside of the effective radius,  $R_e$  shown in Fig. 1. This particular shape becomes more evident in the saturated *i*-band image and is significantly stronger in the south-west direction. Tuned simulations suggest that this particular shape could be produced after a ram pressure stripping event. The gas

removed out from the disc plane in the  $z$  direction can alter the shape of the gravitational potential well, modifying the stellar orbits, thus producing a thicker disc (Farouki & Shapiro 1980; Clarke et al. 2017; Safarzadeh & Scannapieco 2017; Steyrleithner et al. 2020). This phenomenon might explain the peculiar morphology of NGC 4330, with a boxy shape particularly evident in the south-west direction, where the stripping is more efficient. Unfortunately, we lack of stellar kinematical data necessary to further probe this scenario.

### 3.2. Warm gas distribution

The ionised gas distribution of NGC 4330 has been extensively described in Fossati et al. (2018). Here we summarise the main characteristics, referring the reader to that work for a more detailed description. The ionised gas emission mainly comes from the inner regions of the stellar disc, where most of the HII regions are situated (see Fig. 2). The  $H\alpha$  disc is truncated with respect to the stellar disc, indicating that the activity of star formation has been quenched at its edges (Fossati et al. 2018). The north-eastern edge of the star-forming disc is bent to the south in a ‘hook-shaped’ structure (e.g., Abramson et al. 2011), while a few compact and bright HII regions are present just south to the stellar disc at the south-western edge. There is also a very extended, diffuse and low-surface-brightness emission ( $\Sigma(H\alpha) \sim 3 \times 10^{-18} \text{ erg s}^{-1} \text{ cm}^{-2} \text{ arcsec}^{-2}$ ) towards the south of the disc, produced by the gas stripped during the ram pressure episode, indicating that the galaxy is moving northwards on the plane of the sky within the cluster. Associated with the diffuse emission, the VESTIGE  $H\alpha$  image shows a few weak compact regions with a surface brightness over  $\Sigma(H\alpha) \sim 10^{-17} \text{ erg s}^{-1} \text{ cm}^{-2} \text{ arcsec}^{-2}$ , which corresponds to the GHASP detection limit where star formation is probably taking place. Not all the features located out of the plane of the galaxy and above this threshold limit are clearly detected in the monochromatic FP image of NGC 4330, neither in the PUMA data nor in the deeper GHASP data. The bent region at the north-east edge of the disc (labelled A in Fig. 2f) is clearly detected as well as a few regions on the south-west extension of the disc (labelled K, L and M). A few ionised regions have also been detected at the limit of the stellar disc (labelled E, G and F).

## 4. Rotation curves

Rotation curves of galaxies are generally derived using the intensity-peak method (IPM). However, this method hardly works for galaxies with high inclination because the velocity profiles in a given position integrate the whole flux along the line of sight (LoS), thus at different radii along the galactic plane (Sancisi & Allen 1979; Swaters et al. 1997; García-Ruiz et al. 2002; Rosado et al. 2013). To overcome this problem, two different methods are generally used: the envelope-tracing method (ETM; e.g., Sofue et al. 1997, 1999a) and the iteration method (ITM; e.g., Swaters et al. 1997; Takamiya & Sofue 2000; Heald et al. 2006, 2007). We applied these three methods to NGC 4330 following the methodology described in detail in Appendix B. In particular, we invite readers to refer to Appendix B.1 for explanations of position-velocity diagrams (PVDs), which are extensively used in this section on RCs as well as in Sect. 6.

### 4.1. Comparison of the three methods

Figure 3 shows the RCs derived using three different methods: (1) the IPM, (2) the ETM, and (3) the ITM. The RCs obtained with the IPM using both GHASP and PUMA datasets show

that NGC 4330 is rotating as a solid-body inside a radius of  $\sim 30 \text{ arcsec}$ . The output of the fit of Eq. (B.4) (ETM) provides similar terminal velocities reached around  $\sim 30 \text{ arcsec}$  ( $\sim 2.4 \text{ kpc}$ ) as well as similar transition radii between the rising and the flat part of the RCs compared to the IPM method. After this transition, the RCs computed with the ETM method are flat up to the photometric radius  $R_{23,5} \sim 140 \text{ arcsec}$  ( $\sim 11.6 \text{ kpc}$ ), which is represented by the red line in panels a and c of Fig. 3. The approaching and receding sides of the RCs measured with the IPM method start to differ at a radius of  $\sim 30 \text{ arcsec}$  ( $\sim 2.5 \text{ kpc}$ ) and do not have a single point of matching where the two sides overlap until the photometric radius. The rotation velocity obtained for each dataset with the ETM differs by  $8 \text{ km s}^{-1}$ . This number is within the uncertainties due to the differences in resolution between the two instruments and could be partly due to a different threshold for the PVD extraction.

Both datasets show that the RCs derived using the ETM are steeper than those derived using the IPM in the inner regions. This difference is due to the fact that here the contribution of regions along the same LoS but located at different radial distances from the galaxy centre is large, while this is not the case at the edges of the disc where the ETM measures the rotation. Close to the galaxy centre, the width of the PVD is supposed to narrow because along the minor axis the rotation velocity vector lies in the sky plane, and thus its projected component along the LoS is null. Since we do not observe a large decrease in the PVD width in the centre, we conclude that it is mainly due to radial velocity dispersion.

For the GHASP dataset, the RCs derived from the ETM and the ITM have a similar inflexion shape along the transition radius ( $r_t$ ) between the rising and the flat part of the RC (see Fig. 3). Nevertheless, the fit shows that the parameter  $r_t$  differs by  $\sim 5 \text{ arcsec}$  ( $\sim 0.4 \text{ kpc}$ ) using the two methods. For the PUMA dataset,  $r_t$  occurs at a radius  $\sim 9 \text{ arcsec}$  ( $\sim 0.7 \text{ kpc}$ ) larger with the ETM than with the ITM, which makes the RC steeper with this last method (see Fig. 3). Despite the difference between  $r_t$  computed using the ETM and ITM, an acceptable discrepancy between the maximal rotational velocities of  $\sim 8 \text{ km s}^{-1}$  is observed at the photometric radius in the RCs of each dataset.

The three methods consistently show that the rotation of two-thirds of the ionised gas disc of NGC 4330 (i.e. inside a diameter of  $\sim 60 \text{ arcsec}$ ,  $\sim 4.8 \text{ kpc}$ ) can be modelled as a solid rotating body. The same methods have also revealed that the transition between the rising and flat part of the RCs occurs in between  $r_0 \sim 30 \text{ arcsec}$  ( $\sim 2.4 \text{ kpc}$ ) and slightly before the photometric radius.

The IPM allows us to analyse the rotation on both the receding and approaching sides of the galaxy using the pixels within an angular sector of  $\pm 5^\circ$  from the kinematic major axis. The RCs derived using this method show that at the photometric radius the rotation starts to be dominated by streaming motions. This occurs mainly at the south-west of the disc, where the gas has non-circular motions and where the ionised disc is distorted, and hence the projection parameters may be no longer valid in these outer regions. These peculiar motions are not modelled with the other methods. Nevertheless, the ETM and ITM withdraw the effects of LoS to the rotational velocity on the inner disc and allow us to obtain a reliable measure of the maximal rotational velocity of the galaxy, we fix it to the average value of the four velocities given in Table B.1 for the two datasets:  $V_{\text{rot}}^{\text{max}} = 158 \pm 12 \text{ km s}^{-1}$ , the uncertainty being estimated from their standard deviation.

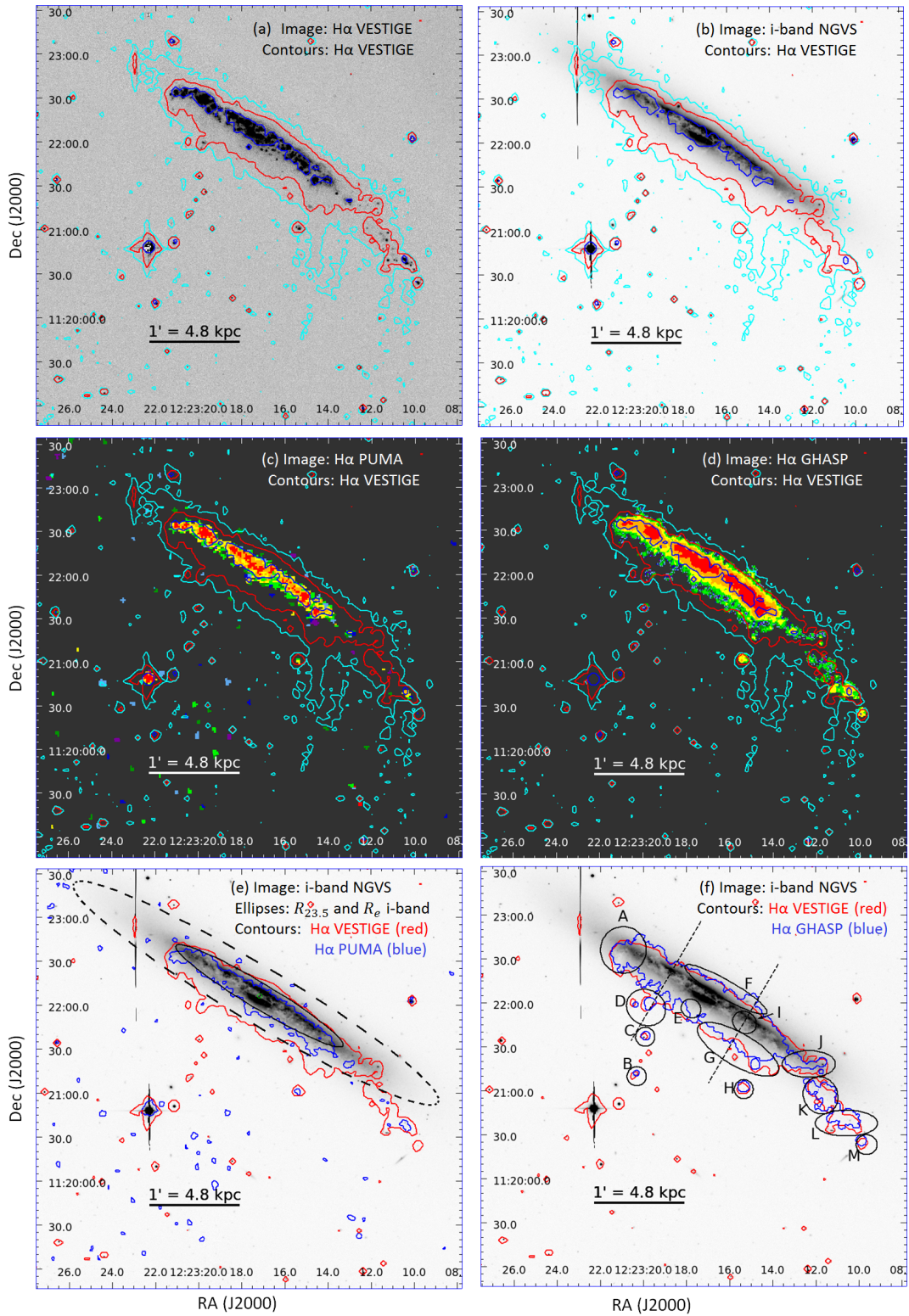


**Fig. 2.** Images of NGC 4330. *Panel a:* full resolution VESTIGE continuum-subtracted  $\text{H}\alpha$  narrow-band image of NGC 4330 in linear scale. *Panel b:* NGVS *i*-band image. *Panels c,d:* PUMA and GHASP FP  $\text{H}\alpha$  monochromatic images, respectively. *Panel e:* NGVS *i*-band image. The dashed black ellipse and the inner ellipse indicate the surface brightness,  $\mu(i) = 23.5$ , and the effective surface brightness,  $\mu_e(i) = 21.5 \text{ mag arcsec}^{-2}$ , respectively, and the green bullet indicates the photometric centre (see Fig. 1). *Panel f:* NGVS *i*-band image with marks on the zones of interest labelled by letters (A to M) and two parallel dashed lines at  $r_0 \sim 30 \text{ arcsec}$  ( $\sim 2.4 \text{ kpc}$ ), which divide the galactic disc into three main regions: north-eastern, central, and south-western (see Sect. 4). The cyan, red, and blue contours in panels a to d show the VESTIGE surface brightness  $\Sigma(\text{H}\alpha) = 0.3, 1.0$ , and  $12.5 \times 10^{-17} \text{ erg s}^{-1} \text{ cm}^{-2} \text{ arcsec}^{-2}$ , respectively. The red contours from panels e and f show the VESTIGE surface brightness  $\Sigma(\text{H}\alpha) = 10^{-17} \text{ erg s}^{-1} \text{ cm}^{-2} \text{ arcsec}^{-2}$ . The blue contours in panel e indicate the surface brightness limit of PUMA,  $\Sigma(\text{H}\alpha) \sim 3.5 \times 10^{-17} \text{ erg s}^{-1} \text{ cm}^{-2} \text{ arcsec}^{-2}$ , while those in panel f show the surface brightness limit of GHASP,  $\Sigma(\text{H}\alpha) \sim 10^{-17} \text{ erg s}^{-1} \text{ cm}^{-2} \text{ arcsec}^{-2}$ .

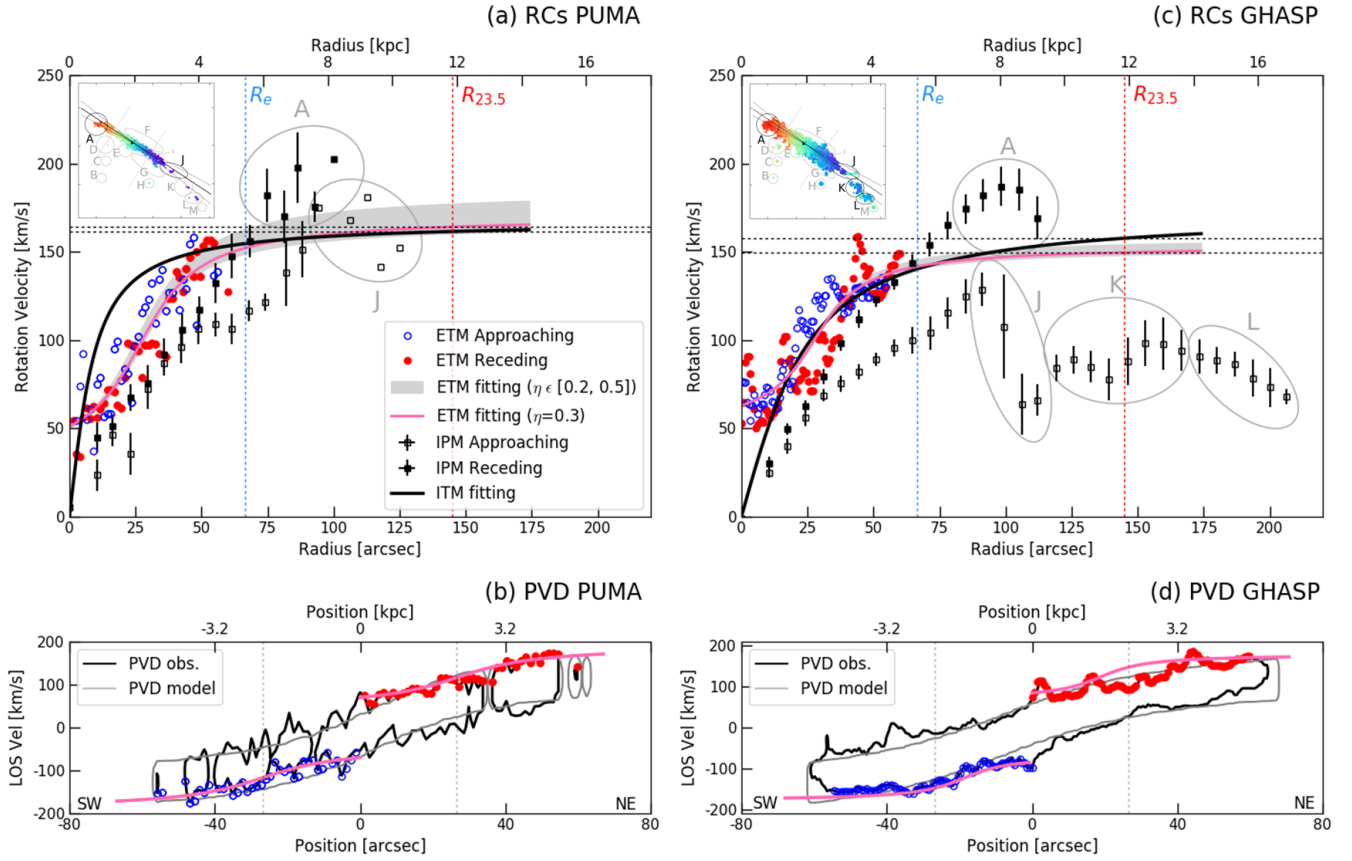


**Fig. 3.** PUMA (panels *a* and *b*) and GHASP (panels *c* and *d*) RCs (panels *a* and *c*) and PVDs (panels *b* and *d*) of NGC 4330. Panels *a,c*: RCs derived using three different methods: the IPM, the ETM, and the ITM (see Appendix B.3 for a further explanation on the methodology). In the case of the IPM (black squares), an azimuthal sector of  $\pm 5^\circ$  in the sky plane has been taken around the major axis to compute the rotation velocities; filled and empty black squares indicate the receding and the approaching sides, respectively. The upper-left insert shows the azimuthal sector and the location of the regions pointed on the RC. For the ETM, the rotation velocities have been derived from the PVD along the major axis ( $z=0$ ), shown in panels *b* and *d*. The terminal velocities are represented by empty blue circles for the receding side and filled red circles for the approaching side; the pink line corresponds to the best fit to these points using  $\eta = 0.3$ , and the shaded area shows the rotation velocity amplitude for  $\eta = [0.2, 0.5]$  (see relation (B.3)). The ITM based on a cylindrical model (described in Appendix B.4) is represented by the black line. Panels *b,d*: PVDs showing the LoS velocities computed with the ETM from which the rotation velocities are computed in the upper panels. On top of the PVD, the filled red and open blue circles indicate the extremal LoS velocities and the pink curve the arctan model fitting those velocities. The red and blue vertical dotted lines in panels *a* and *c* show the photometric and effective radius, and the grey dotted lines in the lowest panels show the position of  $r_0$  (see Sect. 4).

#### 4.2. The dynamical mass

The RC of NGC 4330 is not flat because the gas that is used as a mass-tracer is subject to ram pressure stripping outside the transition radius. Indeed, taking into account its size, morphological type, and maximum rotation velocity, NGC 4330 is an intermediate-mass galaxy that is supposed to have a flat RC (e.g., Sofue et al. 1999b), as previously described in this section by different models. Despite the fact that NGC 4330 is located at  $\sim 0.4$  virial radius from M87 (e.g., Chung et al. 2007), its mass distribution is probably not affected by the cluster environment (Amram et al. 1992) and can be considered as unperturbed. Following Lequeux (1983), the actual dynamical mass of a spiral galaxy that contains a stellar disc, a spherical stellar bulge, and a spherical dark matter halo ranges in the mass interval given by  $M(R) = \alpha R V_{\text{rot}}^2(R)/G$ , where  $G$  is the universal gravity constant,  $V_{\text{rot}}$  the flat rotation velocity, and  $\alpha$  a parameter spanning between the lowest value of  $\alpha = 0.6$  for a galaxy dominated by a flat disc component and the higher value of  $\alpha = 1.0$  if the spherical halo components dominate. Inside the radius  $R_{23.5(i\text{-band})} \sim 11.6$  kpc, using

$V_{\text{rot}}^{\text{max}} = 158 \pm 12 \text{ km s}^{-1}$  and using  $\alpha = 0.8 \pm 0.2$  to be conservative, the dynamical mass of NGC 4330 within  $R_{23.5(i\text{-band})}$  is  $M_{\text{dyn}}(R_{23.5,i\text{-band}}) = 4.4 \pm 0.6 \times 10^{10} M_{\odot}$ . For the same maximum rotation velocity, the mass within the HI radius  $R_{\text{HI}} = 11.3$  kpc is  $M_{\text{dyn}}(R_{\text{HI}}) = 4.9 \pm 1.2 \times 10^{10} M_{\odot}$ . These estimates can be compared to the stellar mass of the galaxy,  $M_{\text{star}} = 5 \times 10^9 M_{\odot}$  (see Table 1).

#### 4.3. Comparison with HI and CO kinematical data

In Fig. C.4 we show the HI velocity fields from Chung et al. (2009) and the RCs we derive from the PVDs. As expected, due to beam smearing effects, the RCs obtained using the minimum and maximum HI surface brightnesses strongly differ. These data are used to compute the ETM RC, which matches fairly well with the  $\text{H}\alpha$  RC, except maybe within the first 2 kpc where the HI velocities have probably been overestimated (see Fig. 4). The comparison between the  $\text{H}\alpha$ , HI, and CO velocity fields are shown in Figs. C.5 and C.6 respectively. The HI velocity field is the most extended with a diameter of  $\sim 282$  arcsec ( $\sim 22.6$  kpc)

**Table 1.** General properties of NGC 4330.

Variable	Value	Ref.
Alternative names <sup>(1)</sup>	HRS 124	a
$\alpha$ (J2000) <sup>(2)</sup>	12 <sup>h</sup> 23 <sup>m</sup> 17.10 <sup>s</sup>	b
$\delta$ (J2000) <sup>(3)</sup>	+11°22′5″.7	b
Type	Scd?	a
Distance	16.5 Mpc	c
Dist. from M87 <sup>(4)</sup>	2.1°/604.8 kpc	TW
D <sub>25</sub>	5.86 arcmin/28.1 kpc	d
i <sub>D25</sub>	11.925 mag	d
V <sub>heliocentric</sub>	1551 km s <sup>-1</sup>	TW
V <sub>rot</sub> <sup>max</sup>	140 km s <sup>-1</sup>	e
PA	59 ± 1°	TW
Morphological Inclination	89.5°	TW
M <sub>star</sub>	5 × 10 <sup>9</sup> M <sub>⊙</sub>	f
M(HI)	4.73 ± 1.04 × 10 <sup>8</sup> M <sub>⊙</sub>	e
M(H <sub>2</sub> )	1.27 ± 0.05 × 10 <sup>8</sup> M <sub>⊙</sub>	g

**Notes.** <sup>(1)</sup>UGC 7456, VCC 630, IRAS 12207+1138. <sup>(2)</sup>Right ascension and <sup>(3)</sup>declination of the galaxy. <sup>(4)</sup>Projected distance for M87.

**References.** TW: This work; a: NED; b: NGVS, Ferrarese et al. (2012); c: Gavazzi et al. (1999), Mei et al. (2007); d: Cortese et al. (2012a); e: Chung et al. (2009); f: Boselli et al. (2015); g: Lee et al. (2017).

from the north-eastern top to the south-western lowest corner. The H $\alpha$  velocity field has been measured on a diameter of  $\sim 205$  arcsec ( $\sim 16.4$  kpc), and exceeds by more than a factor of two the one derived using CO data ( $\sim 94$  arcsec,  $\sim 7.5$  kpc). Despite these differences, which might be partly due to the different sensitivity in the data combined with their different angular resolution (15 arcsec for HI and 6 arcsec for CO), the three velocity fields are comparable indicating a similar kinematics of the three components. We applied the ETM to the <sup>12</sup>CO (2 – 1) data of Lee et al. (2017) and to the HI data of Chung et al. (2009, see Sect. 2.3). From the PVD extracted with a pseudo-slit along the kinematic major axis we computed the terminal velocity using  $\eta = 0.3$ , where  $\eta$  is a fraction of maximum intensity to set the envelope intensity (see Eq. (B.3)), then we fitted the data to the arc-tangent model (Eq. (B.4)) using a least-squares minimisation. The HI, CO, and H $\alpha$  ETM RCs are plotted in Fig. 4, which also includes the H $\alpha$  RCs computed with the ITM and the IPM.

For the HI RC, the ETM fit gave a coefficient of determination  $R^2 = 0.97$ , with  $r_0 = 18 \pm 2$  arcsecond  $r_t = 6 \pm 2$  arcsec, providing a RC with the steepest inner slope, represented by the purple line in Fig. 4. This cuspy inner slope is due to the low HI surface brightness, which is reached thanks to the low-resolution VLA HI data ( $\sim 25$  arcsec; see Sect. 2.3). This low resolution induces strong beam smearing effects and an overcorrection at the lowest HI levels. The ETM provides also a way to estimate of the lowest limit of the RC using only the maximum intensity  $I_{\max}$  (in setting  $\eta = I_{\min} = 0$ ; see Eq. (B.3)). This curve is represented by the purple dashed line in Fig. 4. The interval between the two purple lines delimits all the possible HI RCs that could be computed and gives inner slopes compatible with those obtained at other wavelengths. The maximum HI rotation velocity is  $\sim 10$  km s<sup>-1</sup> lower than those obtained with H $\alpha$  data.

Since the CO is detected only in the inner regions, we extrapolated its ETM RC, using the parameters of the arctan function fitted to the observational data (see Appendix B.3), to compare it with those computed at other wavelengths using the same

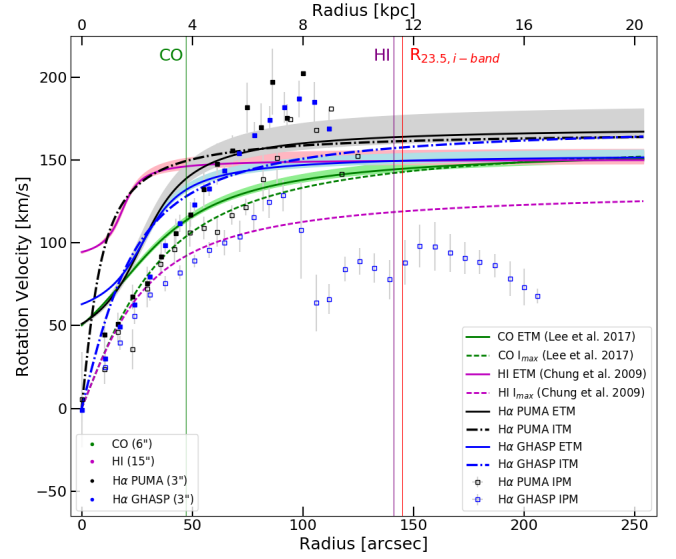


**Fig. 4.** RCs of NGC 4330 derived using the <sup>12</sup>CO(2–1) at  $\lambda = 1.3$  mm data from Lee et al. (2017) (green), the HI ( $\lambda = 21$  cm) data from Chung et al. (2009) (purple), and the FP H $\alpha$  data from PUMA (black) and GHASP (blue). The RCs from CO and HI data were computed using the ETM. The solid lines correspond to the best fit to the points of the terminal velocity using  $\eta = 0.3$ , and the shaded areas show the rotation velocity amplitude for  $\eta = [0.2, 0.5]$  (see relation (B.3)); the dashed lines show the RC computed from the PVD maximum intensity. For comparison, the H $\alpha$  RCs shown in Fig. 3 are also reported on this plot. The green, purple, and red vertical lines indicate the CO extension ( $\sim 47$  arcsec,  $\sim 3.8$  kpc), the HI radius ( $\sim 141$  arcsec,  $\sim 11.3$  kpc), and the outermost photometric radius ( $R_{23.5} \sim 145$  arcsec,  $\sim 11.6$  kpc), respectively. The top-right insert indicates the angular resolution of each dataset.

method. The CO RC is represented by the green dashed line in Fig. 4. The fit of the CO RC, which was obtained with a coefficient of determination  $R^2 = 0.76$ , gave  $r_0 = 19 \pm 10$  arcsec, and the transition between the rising and flat part of the RC at  $r_t = 33 \pm 26$  arcsec. These values are in agreement with those determined for the H $\alpha$  RCs using the same method. At large radii, the CO and the HI RCs match and have values  $\sim 10$  km s<sup>-1</sup> lower than those derived using the H $\alpha$  data. We recall, however, that due to its limited extension, we do not have any observational constrain on the CO RC outside  $\sim 50$  arcsec ( $\sim 0.4$  kpc).

## 5. Kinematical analysis from two-dimensional maps

### 5.1. Velocity fields

Figure 5 shows the velocity field of the ionised gas of NGC 4330 derived from the PUMA and GHASP FP datasets. The velocity fields of both datasets are consistent, they display a rigid body shape inside of a diameter of  $\sim 60$  arcsec ( $\sim 4.8$  kpc) where the isovelocity contours are parallel to the minor axis of the galaxy. We traced on these maps two parallel dashed lines at  $r_0 \pm 30$  arcsec ( $\pm 2.4$  kpc) enclosing this region. Outside this diameter the isovelocity contours become almost parallel to the major axis in the NW hook (region A) and on its counterpart, between regions I and J. However, these maps differ in the southern tail (i.e. in regions K and L; see point 5 hereafter). These last features are the signature of non-circular motions that indicate strong perturbations in the kinematics of the regions affected by the stripping process. The two-dimensional velocity field obtained with high-resolution FP interferometry allows us also to measure

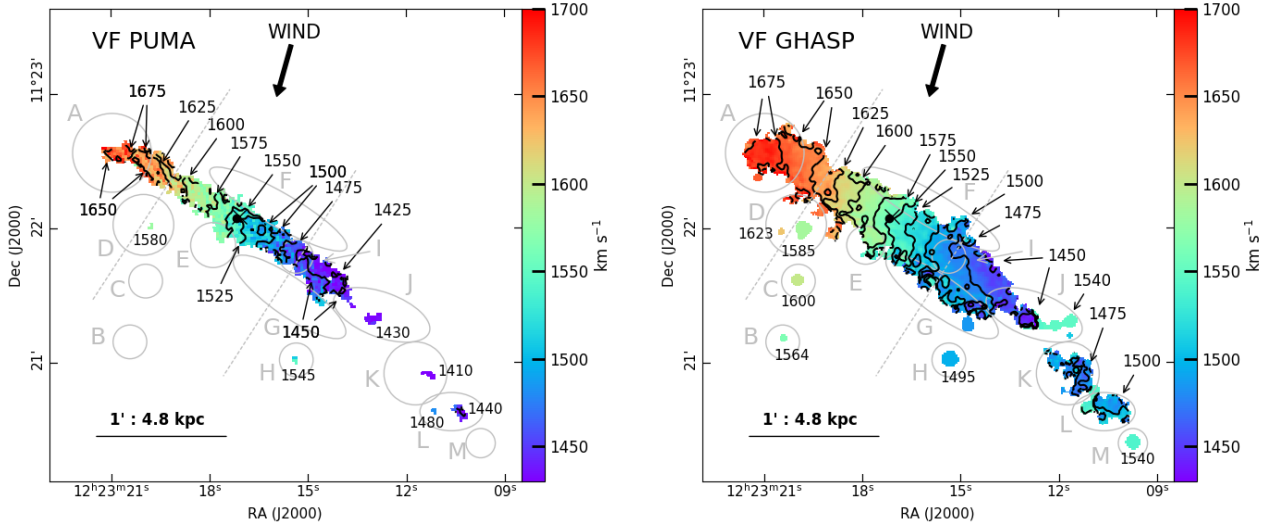


**Fig. 5.** Velocity fields of the ionised gas of NGC 4330 (*left* PUMA, *right* GHASP). The general features of the main disc regions (north-east, central, and south-west), identified by two parallel dashed lines, and the regions with particular features, identified with letters A to H, are discussed in the text. The black bullet and the cross indicate the position of the photometric and kinematical centre, respectively. The black arrow shows the wind direction as derived from the models of Vollmer et al. (2012, 2021).

**Table 2.** Velocities of peculiar regions derived from the PUMA and GHASP datasets.

Region	PUMA			GHASP		
	$V_{\text{rad}}^{(1)}$	$\langle\sigma\rangle^{(2)}$	$V_{\text{res}}^{(3)}$	$V_{\text{rad}}^{(1)}$	$\langle\sigma\rangle^{(2)}$	$V_{\text{res}}^{(3)}$
A	1659	35	−8	1673	19	8
B	...	...	...	1564	9	−41
C	...	...	...	1601	9	−21
D	1580	37	−54	1585	11	34
E	1562	38	20	1579	19	2
F	1543	38	21	1533	20	−2
G	1477	53	48	1493	19	22
H	1548	37	109	1496	21	51
I	1460	37	13	1482	25	3
J	1435	33	19	1542	14	116
K	1412	45	9	1480	15	72
L	1450	38	49	1501	21	99
M	...	...	...	1541	18	139

**Notes.** <sup>(1)</sup>Mean LoS velocity in  $\text{km s}^{-1}$ . <sup>(2)</sup>Mean velocity dispersion in  $\text{km s}^{-1}$ . <sup>(3)</sup>Mean residual velocity in  $\text{km s}^{-1}$ .

the kinematic of the gas in very low-surface-brightness regions. These regions, labelled from A to M, were previously identified in the monochromatic image and they are now identified on the velocity fields of both datasets in Fig. 5. Our data allowed us to measure the LoS velocities of the stripped gas in the southern regions, in region F located on the compression front on the north-eastern side of the disc and in region I on the disc plane. The LoS velocities of all these regions are given in Table 2 and will be further discussed in Sect. 5.4.

We made seven observations. First, the detection and estimation of the LoS velocity of the gas over the galaxy disc, and more specifically inside of regions A, E, F, G, H, I, and J (westernmost part), are robust since derived from independent sets of data with consistent results. Second, the gas inside region A has a radial velocity of  $\sim 1650 \text{ km s}^{-1}$ , which is  $\sim 25 \text{ km s}^{-1}$  lower than that of the disc at the same galactocentric distance.

Third, if we compare the radial velocities in the south-eastern regions of the galaxy with respect to the radial velocities in the plane of the disc, either with respect to their position perpendicular to the plane of the disc or with respect to the direction of the wind as deduced from the direction of the tails and predicted by simulations (e.g., Vollmer et al. 2021), we notice that the gas inside regions B, C, D, and H has radial velocities significantly different ( $\sim \pm 50 \text{ km s}^{-1}$ ) from those measured in the disc from where the gas has been stripped. The radial velocities of the gas regions B, D, and C is lower than that in the disc, while the radial velocity measured in region H is higher by the same amount.

Fourth, despite the fact that they are above the FP detection limit observed in other regions, the detection of ionised gas in regions B, C, D, and M and in the western tail of region J could have been affected by night skyline contamination. Indeed, the night-line subtraction was very difficult because the OH-radical has a strong emission line at  $\sim 6597 \text{ \AA}$  (e.g., Osterbrock et al. 1996), roughly at the same wavelength that the redshifted  $\text{H}\alpha$  emission. On the other hand, the LoS velocity of the gas in region H, which has been probably originated in the approaching side of the disc, is lower and different from the LoS velocity of the gas measured in regions B, C, and D, in the receding side. This difference suggests that these estimates are not largely affected by the residual night skyline emission.

Fifth, ionised gas is detected in regions K and L with similar LoS velocities. A velocity difference of  $\sim 50 \text{ km s}^{-1}$  is observed between both datasets, which could also be due to parasitic night skylines. Thus, despite this difference in the two datasets, these velocities are consistent with streaming motions caused by the stripping process.

Sixth, the gas detected in regions J, K, and H has a velocity similar to that measured at the edge of the rotating disc ( $1450 \text{ km s}^{-1}$ ), suggesting a flat RC.

Finally, Fig. 5 also shows two dashed lines at  $\sim 30$  arcsec ( $\sim 2.4 \text{ kpc}$ ) from the galactic centre. These dashed lines enclose the disc section where the ionised gas shows a rigid-body rotation as indicated by the velocity contours parallel to the minor axis. To the south-west, region I marks the limit where the velocity contours start to become parallel to the major axis. Its counterpart to the north-east is the beginning of the hook shape where

the isovelocities become not parallel to the minor axis. Region I might represent the outer layer of the vertical disc stratification, at the interface with the surrounding medium, where ram pressure begins its action. Since the stripping pressure is not perfectly vertical on the disc, the I region suffers a radial component of the stripping force.

In order to check the highly uncertain velocity of region D gathered with the FP data, we obtained a long-slit spectrum on February 17, 2021, using the low-resolution ( $R = 700$ ) MISTRAL spectrograph installed on the 193 cm OHP (Adami et al. 2018). We took four independent exposures of 15 min each, for a total of 60 min. The exposures were gathered using a slit width 1.9 arcsec oriented north-south to include at the same time region D and the disc of the galaxy. The low-resolution spectrum of region D is shown in Fig. C.2. Because of the night skyline contamination, the  $H\alpha$  line is marginally detected with a signal-to-noise ratio (S/N)  $\sim 2$  and a mean LoS velocity of  $1458 \pm 92 \text{ km s}^{-1}$ , only marginally consistent with the FP measurements of  $1580 \pm 30 \text{ km s}^{-1}$ . Figure C.2 also shows the corresponding MISTRAL spectrum obtained on the galaxy disc north of region D, where the average velocity is  $1629 \pm 46 \text{ km s}^{-1}$ , in very good agreement with the FP data. As for the other extraplanar regions detected in the FP data, the velocity in the stripped gas is lower than that measured in their corresponding regions to the north on the galaxy disc.

The gas stripping process removes the gas from the disc and transfers and dilutes it into the ICM. The only velocity component that we can measure is the one along the LoS. For edge-on galaxies it is straightforward to interpret the LoS velocity as rotation velocity in the galaxy disc plane. The intergalactic wind might change the game, in adding a velocity component related to the direction of motion of the galaxy within the cluster. Nevertheless, in the specific case of NGC 4330, the wind is almost perpendicular to the galaxy disc and has a large component in the sky plane, as suggested by the numerical simulations (see Sect. 7). For these reasons the observed velocities of the gas expelled from the disc are not expected to dramatically change. Thus, the gas continues to rotate outside of the disc and shows the same LoS velocities than those it had before being stripped. Since regions B, C, and D (H) have LoS velocities lower (higher) than their corresponding region in the disc, this suggests that here the gas partly lost its angular momentum during the ram pressure stripping event.

## 5.2. Velocity dispersion

Figure 6 shows the velocity dispersion of the galaxy as measured from the PUMA and GHASP datasets. Following Boselli et al. (2022) we checked that the velocity profiles have a single peak, (i.e. that the barycentric method applied to measure the velocity dispersions does not introduce any strong systematic bias in the results).

At first order, the velocity dispersion of the gas is fairly constant over the disc of the galaxy, with  $\sigma \sim 35 \pm 10 \text{ km s}^{-1}$  and  $\sigma \sim 21 \pm 7 \text{ km s}^{-1}$  for the PUMA and the GHASP data, respectively. The PUMA velocity dispersion is higher than the one measured in the GHASP data because of its reduced spectral resolution. It is indeed difficult to measure velocities far below the instrumental resolution ( $\sigma_{\text{LSF}} = 19.5$  and  $13.1 \text{ km s}^{-1}$ , respectively) as it has been recently discussed in Boselli et al. (2022) in comparing VLT/MUSE data with FP data obtained with GHASP.

At higher spatial frequencies, fluctuations in the velocity dispersion are observed on scales comparable to or larger than the ones set by the seeing. These fluctuations are smoother in the

GHASP data than in the PUMA ones. This is due to the difference in the method used to compute the map (Gaussian smoothing versus Voronoi tessellation, respectively).

Panels c and e of Fig. C.3 show intensity-velocity dispersion diagnostic diagrams and panels a and d the histograms for the intensities and of the velocity dispersions. These diagnostic diagrams are generally used to characterise the dynamics of the ISM in extragalactic giant HII regions (Munoz-Tunon et al. 1996) and also to investigate the dynamic of HII galaxies (Moiseev & Lozinskaya 2012; Carvalho & Plana 2018). Moiseev & Lozinskaya (2012) show a sketch where different features and regions in the plot can be interpreted in terms of (case 1) HII regions (constant velocity dispersion region with high  $H\alpha$  intensity), (case 2) shell (inclined bands in the plot), (case 3) low density turbulent ISM (triangular shape with a base spanning from low to high velocity dispersion and a triangle height ranging from low to moderate  $H\alpha$  intensity).

Shells (case 2) are not observed in the diagnostic diagrams shown in panels c and e, probably because of the lack of spatial resolution for this relatively distant galaxy. The triangular shape distribution of the diagnostic diagram (case 3) is asymmetric, with a deviation towards the lowest velocity dispersions at low intensity and towards larger velocity dispersions at intermediate intensities, indicating the supersonic behaviour of the ISM in NGC 4330. In panel e we selected four areas, represented by ellipses, of different pixel density (from high to low mean pixel density: red, green, dark, and light blue), and identified their locations in the galaxy in panel b. The red pixels with subsonic velocities are mainly located on the outskirts of the galaxy while the dark blue ones, with supersonic velocities, are a little bit on the inner side (case 3). The supersonic green pixels are located along the middle plane of the galaxy while the light blue with the highest intensities (case 1) match with the nucleus of the galaxy and the brightest HII regions. Their velocity dispersion ranges between  $20 \text{ km s}^{-1}$  and  $26 \text{ km s}^{-1}$ .

## 5.3. The residual velocity fields

Two-dimensional residual velocity fields are generally used to optimise the free parameter determination of RCs that are computed from a two-dimensional velocity fields. In general, because the RCs are based on axisymmetric models, a pattern observed on the residual velocity field would be due to incorrect parameter determination. As a consequence, when the free parameters of the RC are optimised, the residual velocity field is pattern-free and the dispersion in the two-dimensional residual velocity is minimum (see Warner et al. 1973; Fuentes-Carrera et al. 2004; Erroz-Ferrer et al. 2012).

The PUMA and GHASP residual velocity maps ( $V_{\text{res}} = V_{\text{LoS}} - V_{\text{mod}}$ ) shown in Fig. 7 were obtained after subtracting the iteration model velocity field ( $V_{\text{mod}}$ ) from the observed one ( $V_{\text{LoS}}$ ). Once we identified the regions presenting a large scatter with the mean velocity dispersion of the residual velocity field, which are not supposed to be in rotation in the plane of the disc, they were masked from the observed velocity field and the axisymmetric model was recomputed. This is because the axisymmetric model is not supposed to be observationally constrained by non-axisymmetric motions.

The residual velocity maps given in Fig. 7 do not show any systematic pattern in the galactic disc and have a velocity dispersion of  $\sigma_{\text{res}} \sim 19 \text{ km s}^{-1}$  for the GHASP dataset and  $\sigma_{\text{res}} \sim 24 \text{ km s}^{-1}$  for the PUMA dataset. The residual velocity is  $\sim 0 \text{ km s}^{-1}$ , suggesting that the adopted cylindrical model (described in Appendix B.4) reproduces the axisymmetric

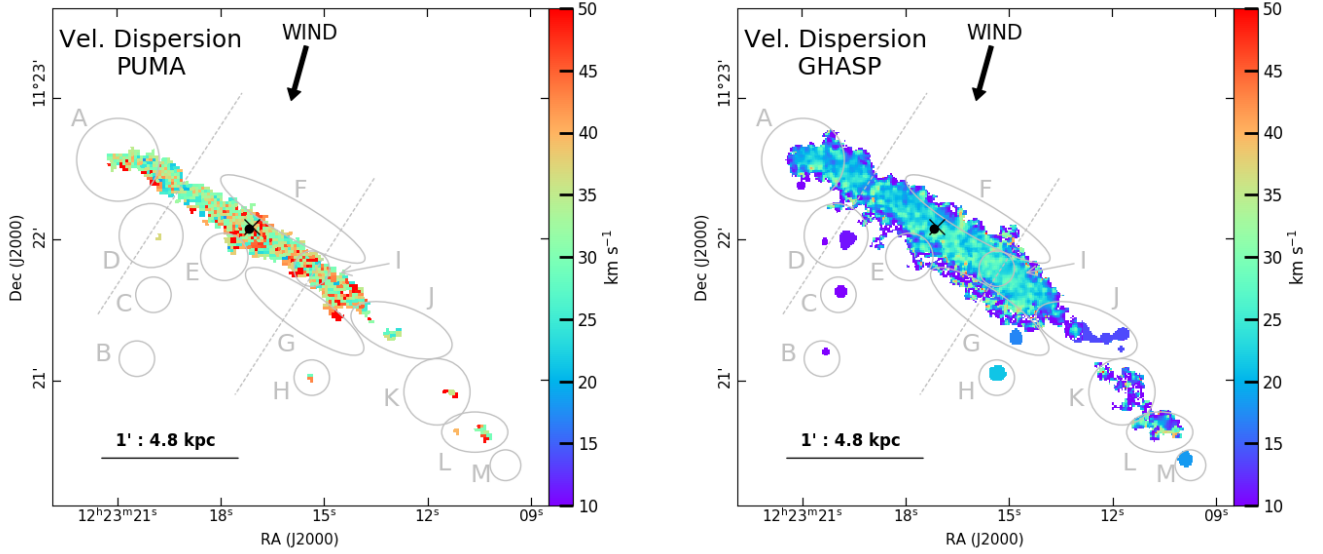


**Fig. 6.** Velocity dispersion fields of NGC 4330 (*left* PUMA, *right* GHASP). The general features of the main disc regions (north-east, central, and south-west), identified by two parallel dashed lines, and the regions with particular features, identified with letters A to H, are discussed in the text. The black bullet indicates the position of the photometric centre. The black arrow shows the wind direction as derived from the models of Vollmer et al. (2012, 2021).

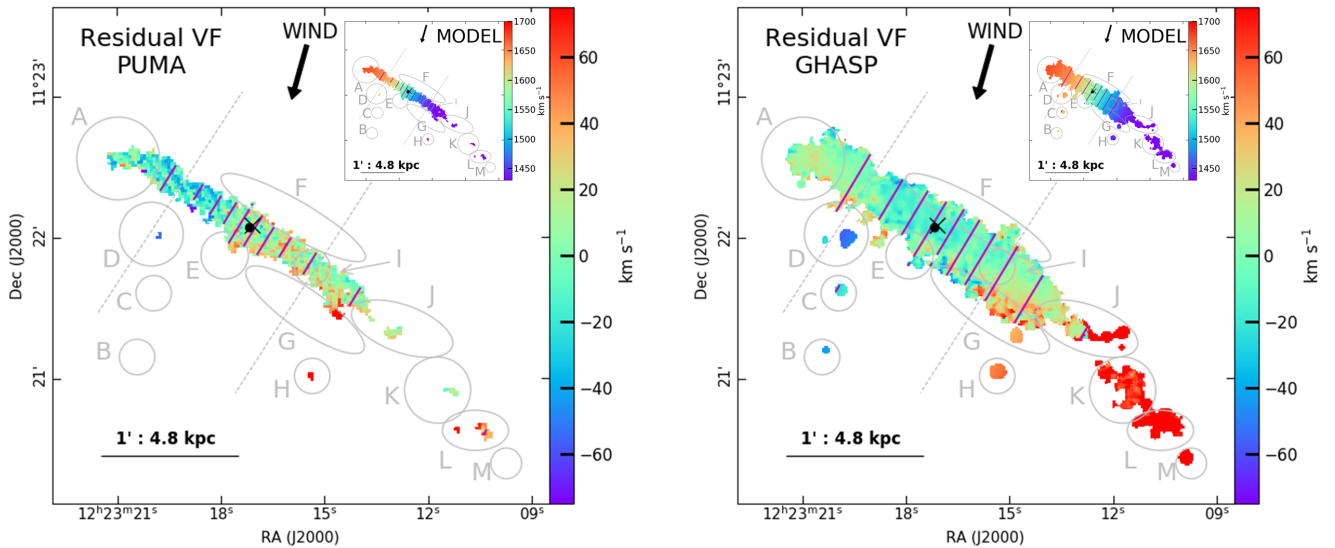


**Fig. 7.** Residual velocity fields obtained after subtracting the velocity field computed from the ITM model data cube (*left* PUMA, *right* GHASP). The model, based on a solid-body rotation, is shown in the inset. The purple parallel lines show the isovelocity contours of the edge-on rotating disc model. The bullet and the cross indicate the position of the photometric and kinematical centre, respectively. The arrow indicates the wind direction as derived from the models of Vollmer et al. (2012, 2021).

rotation of the disc modelled by the RC and its associated parameters well.

An accurate examination of Fig. 7 indicates how the kinematical properties of the various extraplanar ionised gas features created after a ram pressure stripping event differ from those properties predicted by a purely axisymmetric cylindrical model. The most discrepant regions in terms of relative velocity of the gas are regions G, H, and L for the PUMA data and G, H, and from J to M on the south-western side of the galaxy, for the GHASP data. Here the mean gas velocity is  $\sim 50 \text{ km s}^{-1}$  higher than that observed in the model. A less pronounced difference in the same direction is observed in region E ( $\sim 20 \text{ km s}^{-1}$ ), which is located in projection close to the kinematic centre of the disc. On the contrary, the gas inside the regions D (PUMA) and B, C,

D (GHASP) has a mean velocity  $\sim 40 \text{ km s}^{-1}$  higher than that of the cylindrical model. Additional analysis about these individual regions is given in Sect. 5.4.

#### 5.4. Peculiar motions

Table 2 gives the main kinematical properties of the gas in regions A to M. The GHASP data indicate that the gas inside most of these particular regions has a velocity dispersion near to the mean value measured over the galactic disc, and this is probably due to the Gaussian smoothing used to create the map of the velocity dispersion. The PUMA data rather indicate that the gas inside all the same regions has a velocity dispersion higher than the one measured within the galaxy disc, with the higher

velocity dispersions measured in regions E, G, and K. On the other hand, the residual velocity field derived from both sets of data shows that the gas in regions A, E, F, and I follows the rigid-body rotation with a low residual velocity. This result is expected for the gas in regions E, F, and I because they are still associated with the galactic disc but not for the region A, which has been perturbed by the stripping process.

In region A, the velocity contours from both datasets indicate that the gas is rotating with a slight bending with respect to the minor axis. The PVD obtained with the PUMA dataset shows that the gas at the north-east, where the  $H\alpha$  monochromatic map has a hook feature, has higher radial velocities than those expected from the model. For this reason, we could expect that here the gas has a higher velocity dispersion due to non-circular motions, corresponding to high values on the residual velocity map. However, the RCs computed with IPM, which show the gas rotating as a rigid body in region A, do not confirm this result. A decrease in the velocity rotation with respect to the rigid-body rotation is instead observed in the RC and in the residual velocity maps in the south-western side of the galaxy.

Of particular interest is region I, where the GHASP data indicate that the velocity dispersion is  $\sim 5 \text{ km s}^{-1}$  higher than the mean value estimated over the disc of the galaxy. The gas inside region I still follows the rigid-body rotation as indicated by a low residual velocity in both maps. Region I is located at the boundary between the rising and the flat part of the RCs, where the velocity contours in the velocity fields starts to become parallel to the major axis. The PVD shows that here the ionised gas emission start to decrease significantly, and that outside this region the gas starts to rotate slower than expected by the model. Its counterpart on the north-east side of the disc also shows a drop in surface brightness in the PVDs, but outside this region the rotation velocity of the gas seems to increase with respect to the model. In this symmetric region at the north-east of the disc, the gas has no high velocity dispersion and no high residual velocity values. Therefore, the increase in the line width of the gas observed in region I might be due to its acceleration, which is able to remove it from the galaxy disc in the south-west of the galaxy during the stripping event.

Figure 5 shows that the gas inside regions B, C, and D has a lower LoS velocity with respect to those measured in their corresponding positions on the disc plane while region H has a higher one. This means that these four regions rotate slower than their counterparts on the galactic disc. This can also be seen on the residual velocity field (Fig. 7) where the velocities are given in the rest frame of the rotating disc and in which negative (positive) velocities on the approaching (receding) side indicate a lower amplitude rotation outside the plane of the disc. The gas in regions B, C, D, and H does not have a high velocity dispersion, meaning that the wind does not bring a substantial quantity of kinetic energy to those regions. This probably indicates that the gas of these regions had lost angular momentum when it was detached from the galactic disc.

At the southern edge of the galactic disc, the velocity contours are bent with respect to the minor axis. This is particularly evident for the gas associated with region G, where the velocity dispersion and residual velocity increase smoothly with galactocentric distance, reaching their largest value in the detached cloud at the south-western edge of the region. The same cloud at the edge of region G has also a higher LoS velocity than its counterpart on the disc, which means a lower rotation velocity because this cloud is located on the receding side of the disc.

Regions B, C, D, and H show a similar behaviour, they display lower LoS velocities, thus lower rotation velocities because they are approaching to the observer with respect to the galaxy centre. Then, we can infer that the gas inside regions J to M, with a low velocity dispersion but a high residual velocity, has evolved in a similar way as the gas in regions B, C, D, and H (i.e. having lost angular momentum once stripped from the disc). Finally, the gas in region L has a higher velocity dispersion than the one observed around regions K and M. This does not mean that it gets kinetic energy from the wind because the line broadening is probably due to the presence of a star-forming region (see Fig. 2).

## 6. Kinematics of the gas out the plane

In this section we focus on the PVDs at different locations in the galaxy disc, parallel and perpendicular to the major axis of the galaxy, in order to study the kinematics of the gas out of the plane of the stellar disc. Figures 8 and 9, in which we have also located regions A to M, show the PVDs extracted from the PUMA data cube measured along the major and the minor axis, respectively, at different distances from disc plane (e.g., [Epinat et al. 2008a](#); [Rosado et al. 2013](#)).

### 6.1. PVDs along the major axis

Figure 8 shows the PVDs along the major axis at different distances from the disc plane. The pseudo-slits are placed along the  $z$  axis from  $+3.7 \text{ arcsec}$  ( $\sim 0.3 \text{ kpc}$ ) in the northern direction (upwind direction) of the kinematic major axis, up to  $-11 \text{ arcsec}$  ( $\sim 0.9 \text{ kpc}$ ) in the southern direction (tail direction), and they are separated from each other by  $\sim 1.8 \text{ arcsec}$  ( $\sim 0.1 \text{ kpc}$ ; see [Appendix B.1](#)). Figure 8 shows that the rotating gas is less extended along the disc upwind ( $+1.8 \text{ arcsec}$ ), where it reaches  $50 \text{ arcsec}$  ( $\sim 4 \text{ kpc}$ ) in both the north-east and south-west directions, than in the tail ( $70 \text{ arcsec}$  to the north-east and  $60 \text{ arcsec}$  to the south-west). This result is expected in a ram pressure stripping scenario, where the gas is removed outside-in (e.g., [Quilis et al. 2000](#); [Vollmer et al. 2001](#); [Boselli et al. 2006, 2022](#); [Roediger & Hensler 2005](#); [Tonnesen & Bryan 2009](#)).

To identify the main kinematic features resulting from the ram pressure stripping event, we compare the predicted values by theoretical fittings with the observed data. We applied the ETM to each PVD measured along the major axis at different distances from the disc plane. In the left panels of Fig. 8 the best fit to the terminal velocity of each PVD is overlaid on its corresponding plot. In addition, in the context of the ITM, we built a first order approximation data cube model to compute the RC of NGC 4330 (see in [Sect. 4](#)). Here we compare the PVDs from the observational data with the PVDs at the same position obtained from that data cube model in the central panels of Fig. 8. We notice that the cylindrical model follows the emission intensity of the galaxy in velocity and matches with the kinematical behaviour of the major axis PVD.

Some low-surface-brightness plumes of  $H\alpha$  emission were detected on top of the dust lane inside region F. These plumes, which can be seen in the upper two panels of Fig. 8, show an increment in velocity by  $\sim 30 \text{ km s}^{-1}$  breaking the symmetry of the PVDs. If the  $H\alpha$  emission, after being compressed on the front side of the galaxy during the stripping event, is pulled as a whole to the south-west of the stellar disc, these plumes represent gas dragged that is still resisting to change, giving us a clue of the initial state of the disc.

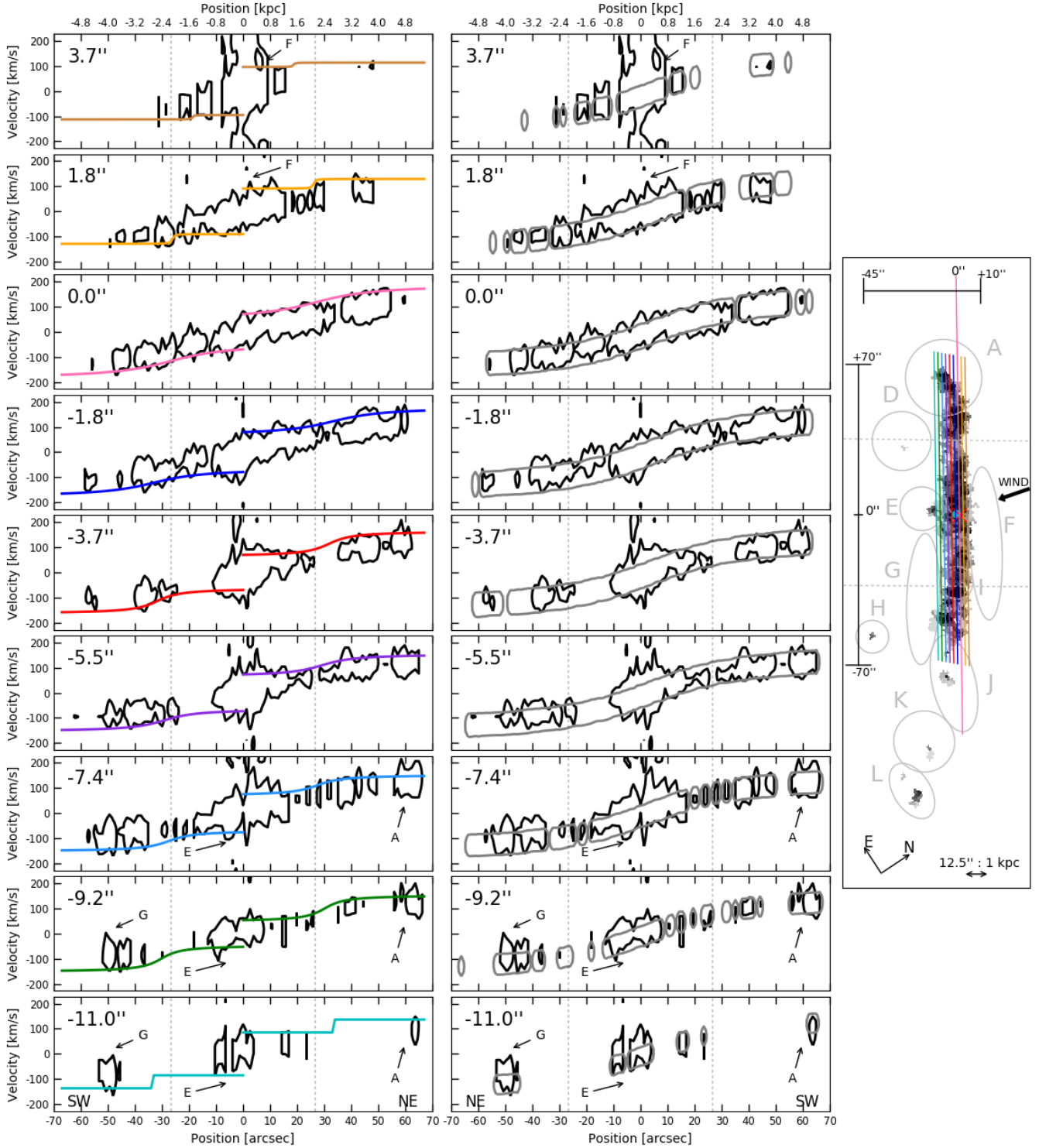


**Fig. 8.** PVDs parallel to the kinematic major axis extracted from the PUMA dataset. The distance of the pseudo-slit from the disc plane along the  $z$  axis (positive to the north) is given in the upper-left corner of each panel. The positions of all the pseudo-slits are shown on the  $H\alpha$  monochromatic map in the *right panel*. From the top at  $+3.7$  to  $-5.5$  arcsec (from  $\sim 0.3$  to  $\sim 0.4$  kpc), the intensity of the contour level is at  $1.5\sigma$ , and from  $-7.4$  to  $-11$  arcsec (from  $\sim 0.6$  to  $\sim 0.9$  kpc) the intensity level is at  $1.2\sigma$ . In the *left panels*, coloured lines overlaid on the PVD represent the best fit of the terminal velocity (Relation (B.3) with  $\eta = 0.3$ ) according to the arc-tangent model (Eq. (B.4)). There is a correspondence in colour between the terminal velocities and the pseudo-slits plotted on the monochromatic map in the *right panel*. In the *middle panels*, the PVDs derived from the data cube model, which was built in the context of the ITM to compute the RC (see Appendix B.4), are overlaid on the observed PVD in grey. All the PVDs extracted from the data cube model are at 8% of the maximum intensity of the model. The two parallel dashed lines are at  $r_0 = \pm 30$  arcsec ( $\pm 2.4$  kpc) and indicate the three main disc regions: north-east, central, and south-west. The different features of interest are indicated with letters A to H.

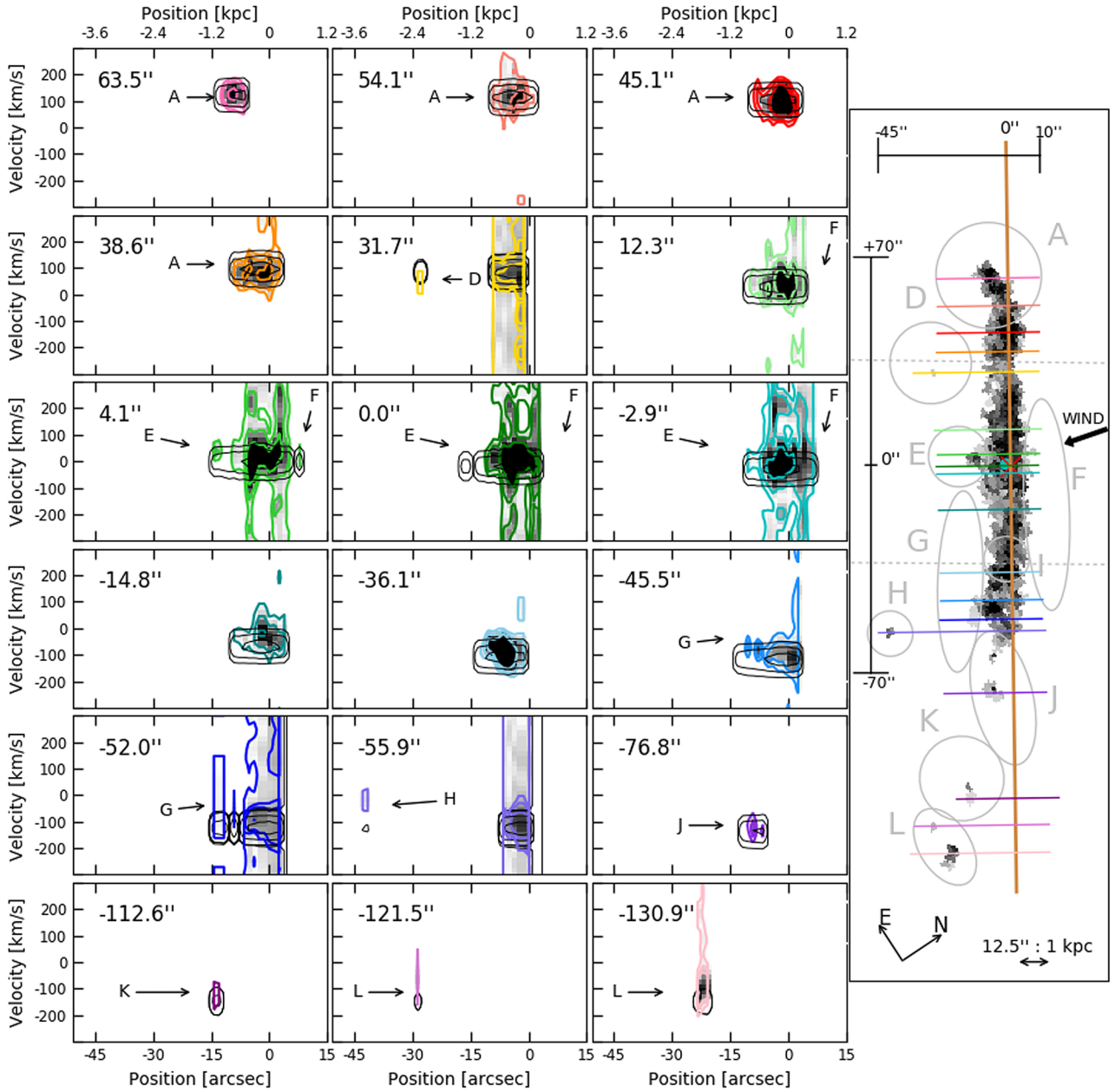


**Fig. 9.** PVDs parallel to the kinematic minor axis obtained from the PUMA dataset. The locations of the pseudo-slits are in the upper-left corner of each panel, and they are traced on the  $H\alpha$  monochromatic map in the *left panel* with colour correspondence. The distance increases from the south to the north of the disc, with zero at the kinematic centre. The black dotted ellipse on the  $H\alpha$  monochromatic map indicates the  $i$ -band  $\mu_e(i) = 23$  mag arcsec<sup>2</sup> isophote. The intensity of the contour levels is 1.3, 1.4, and 1.6  $\sigma$  from  $-45.5$  to  $+63$  arcsec ( $\sim -3.6$  to  $5$  kpc) and 1, 1.1, and 1.25  $\sigma$  from  $-130.9$  to  $-52$  arcsec ( $\sim -10.5$  to  $-4.2$  kpc). The PVDs extracted from the data cube model (black contours) are at 1, 10, and 50% of the maximum intensity of the model.

The PVD along the major axis presents a kinematic symmetry with respect to the kinematic centre without any plume or knot with important variations in velocity with respect to the model. The kinematic major axis matches the bent dust lane in the central region, within a radius of  $\sim 30$  arcsec ( $\sim 2.4$  kpc), enclosed by the vertical dashed lines. As is suggested by the bending of the velocity contours (see Fig. 5), the radial velocities tend to be constant  $\sim 150$  km s<sup>-1</sup> to the south-west, while to the north-east the PVDs show velocities that change by  $\sim \pm 25$  km s<sup>-1</sup> perpendicular to the disc. To the north-east, the gas in region A has a radial velocity of  $\sim 200$  km s<sup>-1</sup>. As indicated by the residual

velocity map (see Sect. 4), although the gas inside region E has a peculiar shape, it rather follows the rotation of the galaxy. On the contrary, the gas in region G has a lower velocity than in the disc.

## 6.2. The lag gradient

Kinematical studies of edge-on galaxies have revealed the presence of a vertical velocity gradient in the RC moving away from the disc plane. This gradient has been observed at optical (e.g., Heald et al. 2006; Rosado et al. 2013; Bizyaev et al. 2017;